Article type: Original Paper

Bound States in the Continuum in Asymmetric Dielectric Metasurfaces

Chaobiao Zhou[1,§], Lujun Huang[2,§,], Rong Jin[3,4,5,§], Lei Xu[6], Guanhai Li[3,4,5*], Mohsen Rahmani[6], Xiaoshuang Chen[3,4,5], Wei Lu[3,4,5] and Andrey E Miroshnichenko[2,*]*

[§]These authors contributed equally.
*Corresponding Author: E-mail: ljhuang@mail.sitp.ac.cn; ghli0120@mail.sitp.ac.cn; andrey.miroshnichenko@unsw.edu.au

[1]College of Mechanical and Electronic Engineering, Guizhou Minzu University, Guiyang, 550025, China
[2]School of Engineering and Information Technology, University of New South Wales, Canberra, Northcott Drive, ACT, 2600, Australia
[3]State Key Laboratory of Infrared Physics, Shanghai Institute of Technical Physics, Chinese Academy of Sciences, 500 Yu Tian Road, Shanghai, 200083, China
[4]Hangzhou Institute for Advanced Study, University of Chinese Academy of Sciences, No.1 SubLane Xiangshan, Hangzhou, 310024, China
[5]Shanghai Research Center for Quantum Sciences, 99 Xiupu Road, Shanghai, 201315, China
[6]Advanced Optics and Photonics Laboratory, Department of Engineering, School of Science Technology, Nottingham Trent University, Nottingham NG11 8NS, UK

It is well established that for symmetry-protected bound states in the continuum (BICs), introducing the broken geometry symmetry in a dielectric metasurface transforms such a BIC into a quasi-BIC (QBIC) with high-quality factor (Q-factor). Typically, the smaller the asymmetry parameter, the larger the Q-factor. However, it is very challenging to fabricate such nanostructures with an ultra-small asymmetry parameter in the experiment due to the limitation of fabrication, thus limiting the measured Q-factor of QBIC. In this work, we demonstrated that BICs can be sustained at Γ point in an asymmetric dielectric metasurface, where the disturbance parameter of quasi-BIC is accurately controlled in the experiment. The unit cell of the metasurface is composed of a dielectric cuboid with an off-centre hole inside it. Such a BIC can be found by moving the

air-hole position in this metasurface. Multipole decompositions and near-field distributions indicate that the toroidal dipole dominates the nature of such a QBIC. Furthermore, we found that such a BIC is robust against the shape of the hole. Besides, two BICs at different wavelengths can be achieved by applying either a rectangular hole or a rectangular lattice. Finally, we presented experimental verifications of BIC types by fabricating asymmetric silicon metasurfaces. Measurement results show that the Q-factor of QBIC can reach almost 5,000. Our results may enrich the library of BICs and find exciting applications in developing high-performance photonics and optoelectronic devices, such as nanolasers, biosensors and enhanced nonlinear harmonic generation.

1. Introduction

Light trapping and manipulation play an important role in developing high-performance nanophotonic-based devices[1], such as ultra-low threshold nanolasers[2], and solar cells[3]. Recently emerging bound states in the continuum (BICs) provides an effective way of achieving perfect light trapping[4–7]. BIC is a non-radiative mode embedded in the radiation continuum with an infinite Q-factor and zero line width[8,9]. From the practical application perspective, BICs must be transformed into quasi-BICs (QBICs) with a high Q-factor so that they can be excited by external excitations. Due to extreme field confinement enabled by QBIC, they have been widely used to enhance the light-matter interaction at the nanoscale and led to many exciting applications, such as in nanolasers[10–14], biosensors[15–17], electro-optic modulators[18], nonlinear optical devices[19–22], and strong coupling[23–27]. Also, the topological nature of BIC[28] enables researchers to design chiral metasurface[29–33] with nonlocality and generate orbital angular momentum[34].

Among the BIC family, the symmetry-protected BIC (SP BIC) is the most common and is easy to realize experimentally[35]. For practical application, one should break the unit cell's

symmetry by removing or adding part of the geometric structure in the metasurface to transform such a BIC into a QBIC with a high Q-factor. Typical examples of broken-symmetry in unit cell include split-rings[36,37], asymmetric nanorods[21,38–40], notched cubes[20,41,42], and notched disks[43–45]. It is noted that the smaller the asymmetry parameter, the larger the Q-factor. Thus a larger asymmetry parameter is always accompanied by a lower Q-factor. In practical experiments, fabricating nanostructures with an ultra-small asymmetry parameter is very challenging thus limits the measured Q-factor. Although significant progress has been made on both fundamentals and applications of BICs in the past ten years, some open questions remained unanswered: Can non-radiative BIC sustain in a dielectric metasurface if its symmetry is broken? Can the perturbation parameter that governs the Q-factor of QBIC be precisely controlled?

In this work, we present a theoretical prediction and experimental demonstration of the existence of BIC at Γ point in asymmetric metasurfaces, and the disturbance parameter of excited quasi-BIC can be accurately controlled in the experiment. Such metasurfaces are made of an off-centre hole that is embedded in a square Si nanodisk. It is found that BIC can be constructed at a critical position when the air-hole moves along the *x*-axis, *y*-axis and diagonal, respectively. Multipole analysis and the near-field distribution confirm that such a BIC is mainly governed by toroidal dipole (TD). Moreover, we find that such a BIC is robust against the shape of the air hole, providing an alternative way of realizing high Q-factor resonances. We also demonstrated that two BICs at different wavelengths can be attained under different polarization illumination by using a rectangular hole inside the square nanodisk or rectangular lattice. Finally, we fabricated such asymmetric silicon metasurfaces and demonstrate high-Q resonances enabled by TD-dominated QBIC. The highest Q-factor observed in the experiment can reach almost 5,000. Our results extend the existence form of BIC and provide new routes for enhancing light-matter interaction with such a high Q-factor optical resonance.

2. Results and discussion

The metasurface is composed of silicon nanodisks with an air hole arranged in a square lattice, as shown in **Figure** 1. The period of unit cell *P* is 800 nm, the side length of nanodisk *L* is 700 nm, thickness *h* equals 220 nm, and the radius of air-hole *r* equals 125 nm. The air hole's offset distance from the nanodisks' centre is marked *d*. The optical properties of the metasurface are evaluated by the finite element method with commercial software COMSOL Multiphysics, rigorous coupled-wave analysis (RCWA) and finite-difference time-domain method (FDTD Solutions). The refractive index of n=3.48 is used for silicon. In previous studies[46–48], we have demonstrated that such metasurfaces support a number of leaky mode resonances that govern their optical response (i.e., reflection, transmission, absorption). These resonant modes are characterized by the complex eigenfrequencies $\omega = \omega_0 - i\gamma$, where ω_0 and γ correspond to the resonant frequencies and radiative decay rates, respectively. According to previous studies, such metasurfaces supports magnetic dipole QBIC when the air-hole moves away from the center of cuboid[19,49]. However, in this work, we mainly focus on the leaky mode, whose eigenfield profile is shown in **Figure** 1(b). In addition to that, **Figure** 1(c) shows the Q-factor of this mode versus off-set distance for dielectric metasurfaces without and with the substrate. For the free-standing metasurface, it can be seen the Q-factor increases with the increasing offset distance, and reaches a maximum value of 3.16×10^9 at d=95.1 nm. The Q-factor can reach infinity for the extremely enhanced numerical resolution, confirming the existence of a non-radiative BIC. The eigenfield profile of this ultrahigh-Q mode is shown in **Figure** 1(b). Further increasing *d* results in a decreased Q-factor. If a glass substrate (n=1.45) is introduced underneath, the Q-factor's maximum value drops almost three orders due to the reduced refractive index contrast between the metasurface and substrate, bringing energy leakages into the glass substrate.

To confirm the existence of such a BIC, we calculate the reflection spectra mapping for the free-standing metasurface versus offset distance and incident wavelength under *x*-polarized plane wave illumination, as shown in **Figure** 1(d). Indeed, it can be seen that the resonant peak shows vanished linewidth at d=95.1 nm due to the negligible coupling between the incident wave and the BIC. The existence of BIC is also confirmed in the glass substrate case by plotting the reflection mapping (see **Figure** S1).

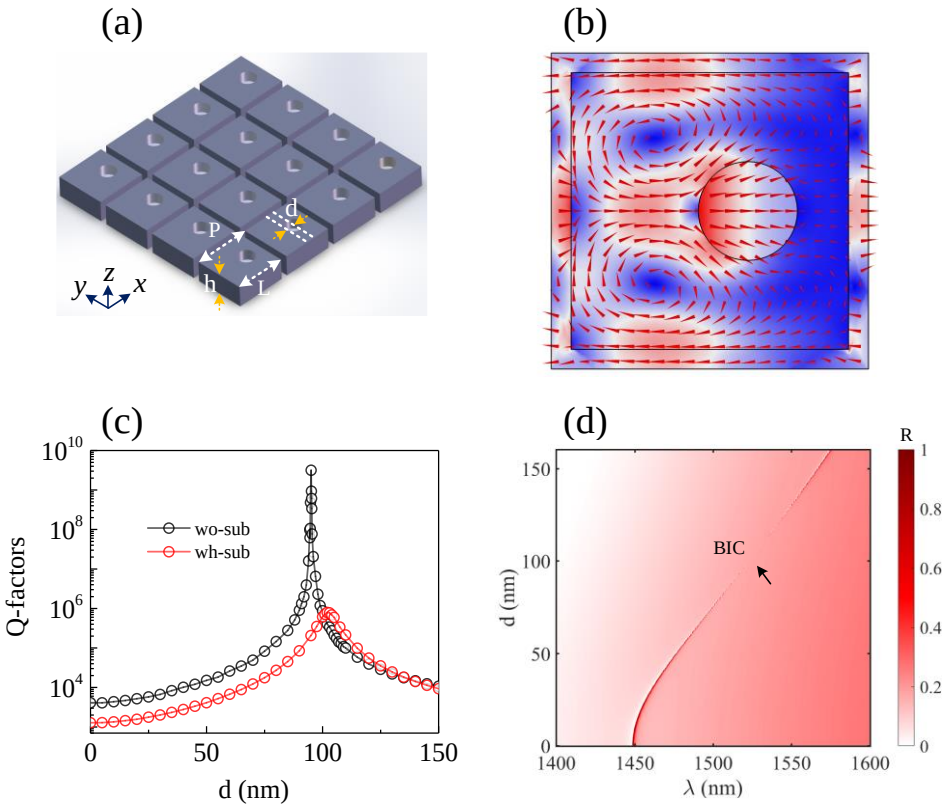

Figure 1. (a) Schematic of the proposed metasurface. The period *P* is 800 nm, the side length of nanodisk *L* is 700 nm, thickness *h* is 220 nm, and the radius of air-hole *r* equals 125 nm. The air-holes offset distance from the nanodisks' centre is marked *d*. (b) The eigenfield distribution and field vector for BIC mode. (c) The Q-factors with respect to the off-set distance d for free-standing (black) and glass substrate (red) cases, respectively. (d) The reflection mapping versus both the offset distance and wavelengths for free-standing metasurface.

To reveal the nature of such a QBIC, we perform the multipole decomposition[50–52] (See Section 1 in the SI). For the sake of simplicity, the offset distance *d*=30 nm is used as an example

to discuss the resonance properties of QBIC, the calculated reflection spectrum is shown in **Figure** 2(b), and the resonance wavelength is 1464 nm. **Figure** 2(c) exhibits the scattered power of multipole components. It is obvious that the TD response dominates this mode. Also, a mild contribution comes from the magnetic quadrupole (MQ), because pair of counter-oriented magnetic dipoles induce TD and MQ. Further analysis of the TD indicates that the *x* component of TD plays a major role, as confirmed in **Figure** 2(d). In fact, the TD response nature is also evidenced by its near-field distribution shown in **Figure** 1(b). The two field vector distributions with opposite directions, observed in the *x*-*y* plane, excite opposite magnetic dipoles along the *z*-axis. Combining the incident light with *x* polarization, a circular magnetic loop in the *y*-*z* plane excites a strong magnetic TD along the *x*-axis.

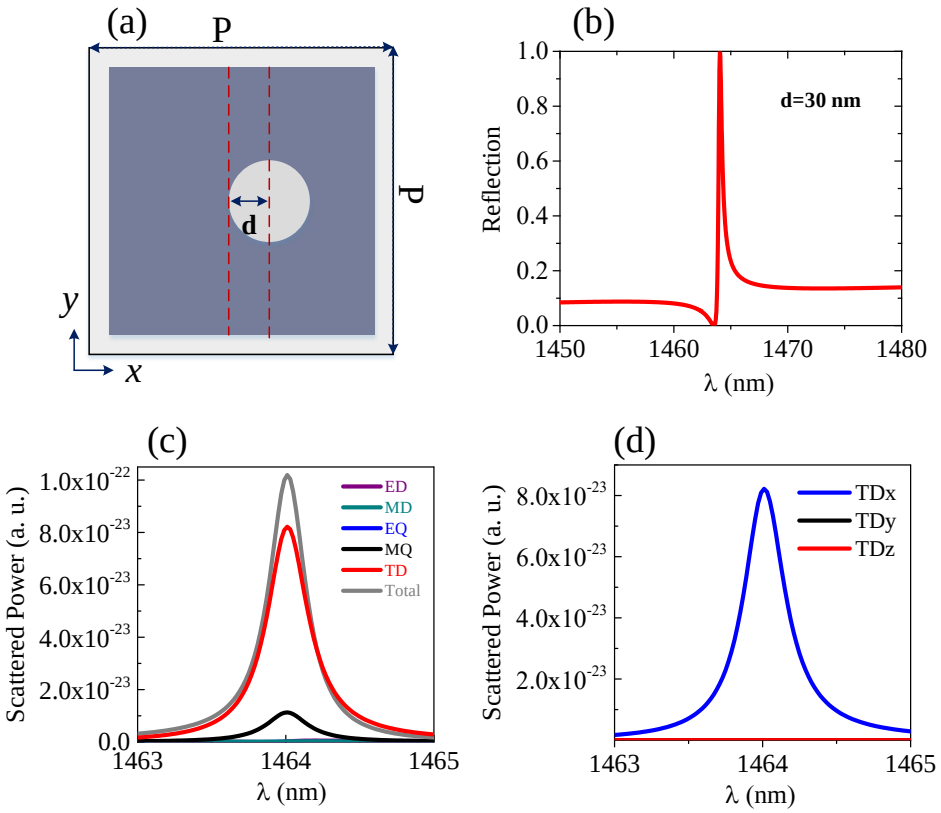

Figure 2. (a) Top view of the unit cell with off-centre hole. Here, the *P* is still 800 nm, *L* is 700 nm, *h* is 220 nm, *r* equals 125 nm, and d=30 nm. (b) The corresponding reflection spectrum. (c) The calculated scattering power of different multipole moments. (d) The scattered power of multipole components of the toroidal dipole.

It is interesting to note that such a BIC mode is robust against the shape of the air hole. When the circular hole is replaced by a square hole with a side length of 220 nm [**Figure** 3(a)], this BIC is still discovered, as shown in **Figure** 3(b), and the Q-factor reaches 3.8×10^9 at d=112.4 nm. Its eigenfield distribution is similar to the case of the circular hole, therefore this QBIC mode is also dominated by TD response. Further, we consider an even more general case by rotating 30 degrees of the square hole, as schematically drawn in **Figure** 3(d). Still, one can observe this BIC from **Figures** 3(e)-(f) when the rotated square hole moves along the *x*-axis. Multipole analysis indicates that all of these QBICs are dominated by TD (See **Figure** S2). Thus, we can safely conclude that such a BIC is insensitive to the air-hole shape, and the Q-factor of the BIC only depends on the relative position of the air-hole, which can be precisely controlled in a real sample fabrication, and provides an effective route for the realization of a high Q-factor resonator.

Excerpt for weak-shape dependence, we find that such a BIC also exists when the air-hole moves along the diagonal of the square lattice, as shown in **Figure** 3(g). From **Figure** 3(h), it can be found that Q-factor reaches a maximum of 2.5×10^9 at dx=70.9 nm. Its eigenfield and field vector, as shown in **Figure** 3(i), are symmetrically distributed along the diagonal. However, compared to the previous BIC, the electric field vector shows a very distinct circular distribution in the lower-left region of the air hole, indicating that magnetic dipole (MD) plays a critical role in forming of this BIC. In addition, there is an unobvious and inverted circular field vector distribution in the upper right corner, signifying that TD also makes significant contributions to the BIC. Multipole decompositions show that MD and TD's contributions compete with each other in this mode. TD plays a dominant role when the air hole is close to the nanodisk's centre. MD's contribution gradually increases when the hole is gradually moved away from the center along the diagonal. Their contributions are comparable at dx=45 nm, and the response of MD gradually dominates as dx increases (see **Figures** S3 and S4). It is noted that TD always

dominates this mode for moving air hole along the *x*-axis due to stable symmetric field distributions (see the comparison from Figure S4). In addition, the extinction ratio of the resonance peak reaches maximum under -45° polarization light when the air-hole is moved along the diagonal. Only part of the light is coupled into the device for other angles of incident light (see Figure S5).

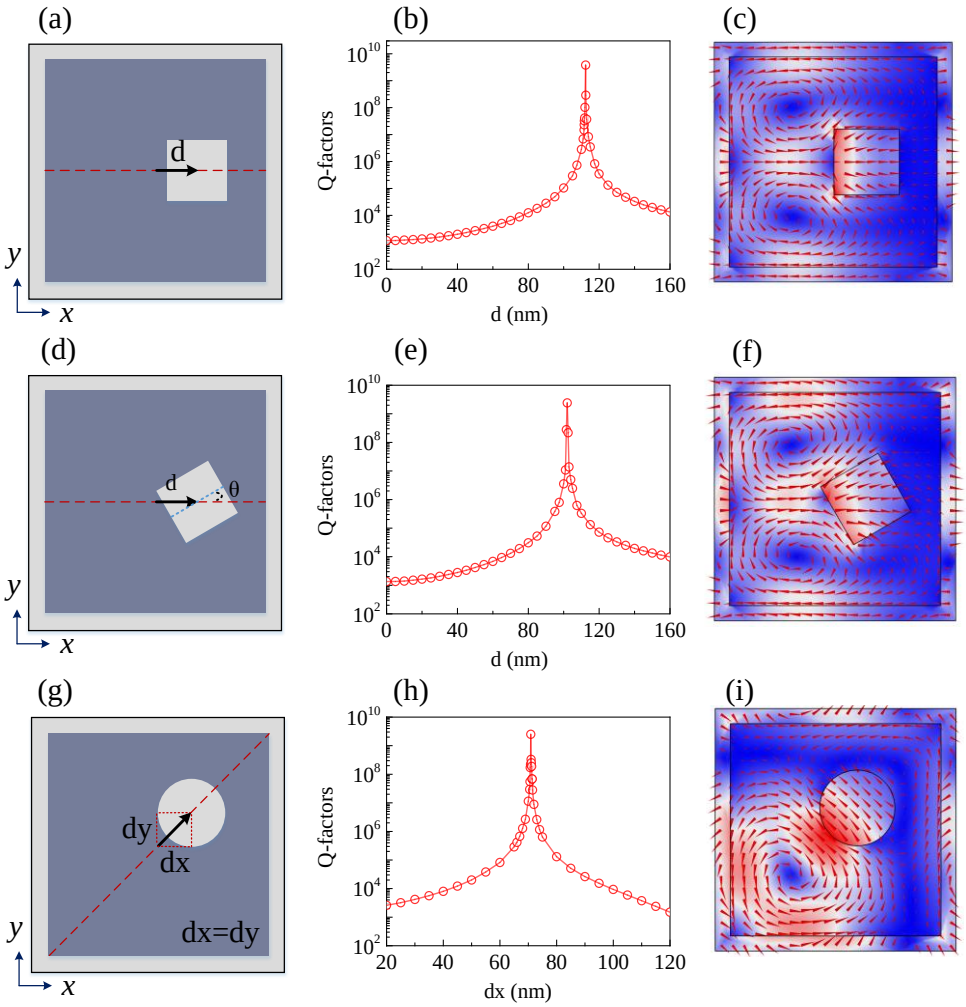

Figure 3. (a),(d) Schematic diagrams of the square hole and rotated 30 degrees moving. (b),(e) Variation of Q-factor with offset distance d. (g) Schematic diagram of the air-hole moving along the diagonal with d*x*=d*y*. (h) Variation of Q-factor with d*x*. (c),(f),(i) The eigenfield and field vector distribution for BIC position. Here, the *P* is still 800 nm, *L* is 700 nm, *h* is 220 nm, *r* equals 125 nm, and the side length of the square-hole *l* is 200 nm.

As can be seen in the above discussion, TD-dominated BIC is observed when the air hole is moved along the *x*-axis. Since the current metasurface has a square lattice and square nanodisk with an air hole, one should expect the same BIC with identical resonant wavelength and Q-factor at the same position d*y*=d*x*=d if air-holes move along the *y*-axis. We employ two strategies, applying either a rectangular air-hole or rectangular lattice, to distinguish the BICs at different wavelengths with two different configurations. **Figure**s 4(a)-(c) show the case of a rectangular hole inside a square nanodisk arranged as a square lattice. **Figure** 4(b) shows that one BIC appears at d*x*=34 nm when the air hole is moved along the *x*-axis. However, the other BIC occurs at d*y*=102 nm for *y*-polarized light. Besides, their corresponding resonant wavelengths are obviously different, as shown in **Figure** 4 (c). It is worth pointing out that when adjusting the relative lengths and widths of rectangular air holes, the positions of the BIC and the resonance wavelengths will keep approaching, and the modes overlap completely when the lengths and widths are the same. We also discuss the properties of QBIC for the rectangular hole, and calculate the resonance spectra, multipole contributions, eigenfields and field vectors for d*x* and d*y* of 160 nm, respectively. The results confirm that QBIC indeed arises from the same BIC (see **Figure** S6). Another strategy for implementing two BICs at different wavelengths is to replace the square lattice and square nanodisk with rectangular lattice and rectangular nanodisk while keeping the gap between the nanodisks still at 100 nm. The structural diagram is shown in **Figure** 4(d). The BICs are observed at different offset distances when moving the circular hole in the *x* and *y* directions, respectively. The resonant wavelengths are also obviously different, as illustrated in **Figure** 4(e) and (f). The multipole and eigenfield of the QBIC modes are also calculated for the two schemes, confirming the TD nature of the two BICs (see **Figure** S7). Here, it is necessary to comment that two BICs with different wavelengths happening at different polarization may suggest a way of realizing two high-Q resonances at two wavelengths.

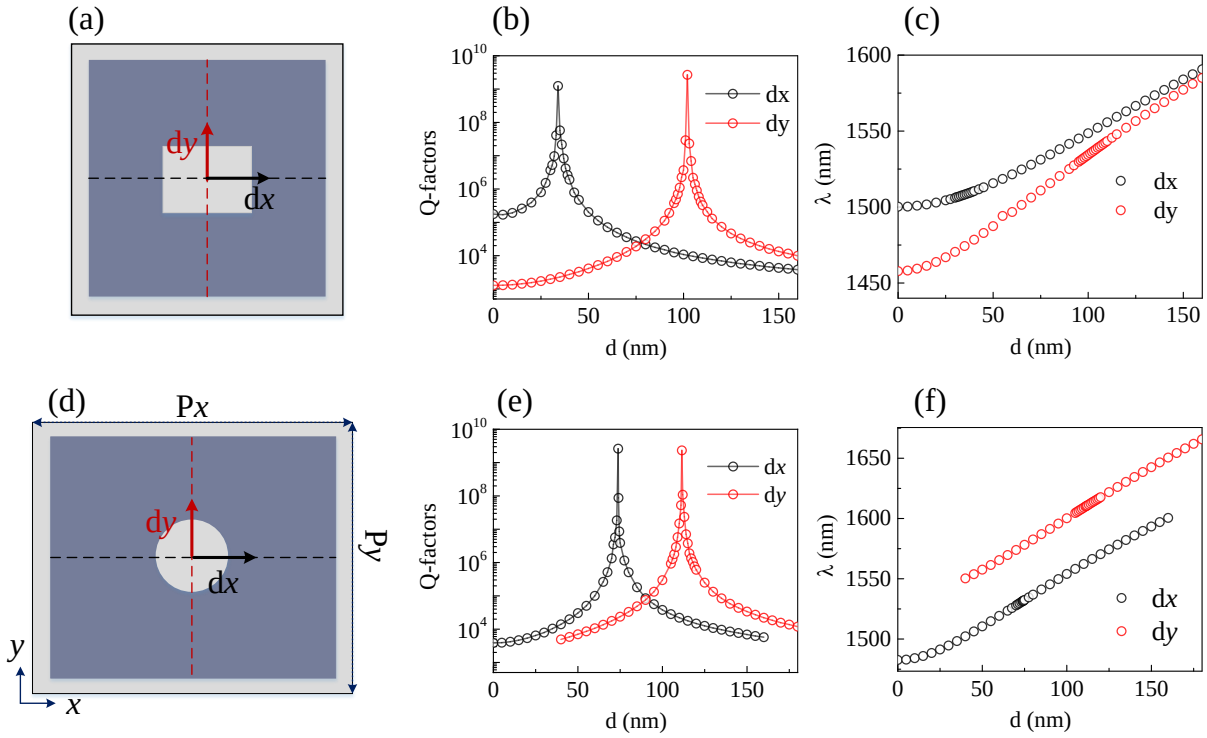

Figure 4. (a) Schematic diagram of the unit cell of the rectangular hole, the length of the hole is 250 nm, the width is 160 nm, the width of the nanodisk is still 700 nm, and the period is 800 nm. (b),(c) Q-factors and resonance wavelengths when the hole is moved along the *x* or *y* direction, respectively. (d) Schematic diagram of the unit cell of a rectangular nanostructure with P*x*=850 nm, P*y*=800 nm, the long side of the nanodisk L*x*=750 nm, the short side L*y*=700 nm, and the radius of the air hole *r*=125 nm. (e),(f) Corresponding to the Q-factors and resonance wavelengths when the hole is moved along the *x* or *y* direction, respectively.

Finally, we perform a relevant experiment to confirm these TD BICs, and the device schematic is shown in **Figure** 5(a). The metasurfaces are fabricated through electron-beam lithography (EBL) and inductively coupled plasma (ICP) etching techniques (see Methods Section). We fabricate six samples of nano-holes moving from *d*=50 nm to *d*=150 nm along the *x*-axis in steps of 20 nm. The scanning electron microscopy (SEM) image of the fabricated sample is shown in **Figure** 5(b). Compared to the free-standing metasurface, the maximum Q-factor for a glass substrate case reduces three orders of magnitude due to mode leakage into the substrate. Cross-polarization measurement is applied to measure high-Q resonance[53,54] (See

methods section). The measured scattering spectra are plotted in **Figure** 5(d). The resonance spectra are in excellent agreement with the calculated results in **Figure** 5(e). By applying the standard Fano fitting procedure[55], the experimental Q-factors of different off set distances are retrieved and shown in **Figure** 5(f). All of the measured Q-factors are between 1,000 and 5,000. The largest value is up to 4.99×10^3. The lower observed Q-factor compared to theoretical prediction can be mainly attributed to the imperfect vertical sidewall of the air-hole (see Figure S10 and Table S1). In addition, the residual difference of the Q-factor may be contributed by the roughness, nonuniformity of the nanodisks and some incidence angles. We expect to achieve a higher Q-factor when the fabrication process and characterization system are further optimized.

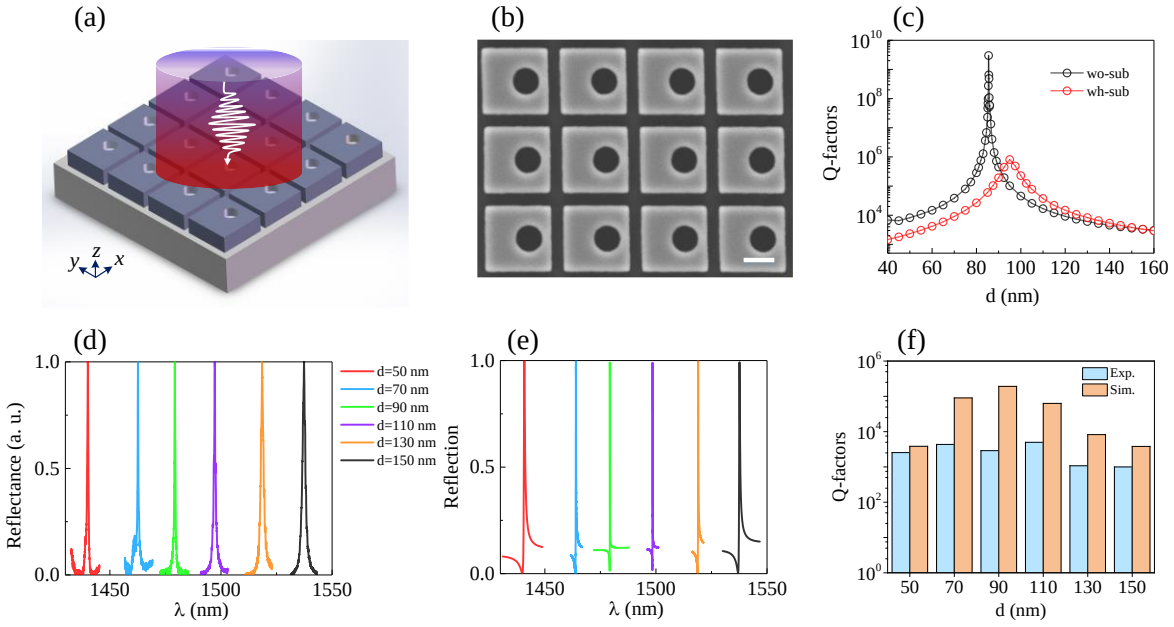

Figure 5. (a) Schematic of silicon metasurface, *P*=800 nm, *L*=680 nm and *r*=135 nm. (b) The top-view SEM image of the fabricated nanodisk array, the scale bar in white is 300 nm. (c) The Q-factors with respect to the off-set distance *d* for free-standing (black) and glass substrate (red) cases, respectively. (d),(e) The measured and calculated (SiO_2 substrate) reflection spectra, change the offset distance from 50 nm to 150 nm. (f) The measured and calculated Q-factor for different parameters *d*.

3. Conclusion

In summary, we demonstrated the BIC in the asymmetric all-dielectric metasurface, which is composed of a square array of Si nanodisks with an off-centred penetrating air hole. Such BICs are sustained only when the air-hole moves along the *x*-axis, *y*-axis, and diagonal axis. Multipole decomposition on the QBIC suggests that this mode is dominated by the *x*(*y*) component of TD if the air-hole is moved along *x*(*y*)-axis. Besides, we found that this type of BIC shows great robustness against the air-hole shape, which may remove the obstacles of fabricating a high-Q resonator due to fabrication imperfection. In addition, we demonstrated that it is possible to build two BICs at two different wavelengths by transforming a square lattice or square hole into a rectangular lattice or rectangular hole. Finally, we also experimentally demonstrate this type of BIC in asymmetric silicon metasurfaces based on the SOI wafer. The Q-factor reaches a maximum value of 4.99×10^3, which is limited mainly by scattering losses arising from fabrication imperfection. Higher Q-factors may be achieved by optimizing fabrication processes and characterization systems. Our results provide a route to achieve the high Q-factor resonator with better performance applied in nanolasers, optical switching, biosensing, and so on.

4. Experimental Section

Electromagnetic Simulations: The Q-factors and eigenfield of the metasurface are calculated by commercial software Comsol Multiphysics based on the finite-element method (FEM). The reflection mappings are calculated by rigorous coupled-wave analysis (RCWA). And the finite difference-time-domain method (FDTD Solution) is used to calculate the reflection spectra and scattered power of different multipoles.

Fabrication: The metasurfaces are fabricated on a silicon-on-insulator (SOI) wafer with a 220-nm top silicon layer and 2-um-thick buried layer, and the thickness of the Si substrate is about

700 μm. Firstly, a clean SOI wafer is coated with a resist layer (ZEP520). Then, the patterns are defined in the resist by the EBL tool. After being carefully developed and fixed, the patterns are transferred to the silicon diaphragm by the ICP technique. Finally, the remaining resist is removed with the Nmethyl-2-pyrrolidone (NMP) liquor (see **Figure** S8).

Optical Characterization: Spectroscopic measurements are made using a home-built microscope spectroscopy system (see **Figure** S9). Cross polarization measurement is applied to measure the high-Q resonant modes from the fabricated metasurfaces. A super-continuous laser (NKT SuperK COMPACT), which has a broad spectrum ranging from 450 nm to above 2000 nm, first passes through the long pass filter, linear polarizer, and beam splitter and then is focused on the sample with an objective lens 10X. A long-pass filter is used to eliminate the impact of light on unused wavebands. The reflected signal from the sample is collected by a spectrometer (ANDOR SR750) with a grating of 900l to reach a theoretical resolution of 0.06 nm. A pair of strictly orthogonal polarizers are placed at the front and the end of the light path, to introduce cross-polarization, which can efficiently decrease the impact from background reflection and promote the relative intensity of the signal.

Supporting Information

Additional supporting information may be found in the online version of this article at the publisher's website.

Section 1-Multipole Decomposition

Figures S1-11

Table S1

Acknowledgements

C. Zhou was supported by the National Natural Science Foundation of China (12004084 and 12164008), the Guizhou Provincial Science and Technology Projects (ZK[2021]030), and the

Science and Technology Talent Support Project of the Department of Education in the Guizhou Province (KY[2018]043]). L. Huang and A. E. Miroshnichenko were supported by the Australian Research Council Discovery Project (DP200101353) and the UNSW Scientia Fellowship program. L. Huang was also sponsored by Shanghai Pujiang Program (22PJ1402900). R. Jin, G. Li and X. Chen were supported by the National Key Research and Development Program of China (2018YFA0306200 and 2017YFA0205800), National Natural Science Foundation of China (61875218, 61991440, and 91850208), Youth Innovation Promotion Association of the Chinese Academy of Sciences (2017285), Strategic Priority Research Program of Chinese Academy of Sciences (XDB43010200); Shanghai Rising-Star Program (20QA1410400), Natural Science Foundation of Zhejiang Province (LR22F050004), Shanghai Science and Technology Committee (20JC1416000), and Shanghai Municipal Science and Technology Major Project (2019SHZDZX01). M. Rahmani appreciates the support from the Royal Society and the Wolfson Foundation.

Conflict of Interest

The authors declare no conflict of interest.

Keywords: bound state in the continuum, high Q-mode, dielectric metasurface

Received: ((will be filled in by the editorial staff))
Revised: ((will be filled in by the editorial staff))
Published online: ((will be filled in by the editorial staff))

References

[1] K. A. Femius, A. Andrea, P. Albert, *Science (80-.).* **2015**, *348*, 516.

[2] R.-M. Ma, R. F. Oulton, *Nat. Nanotechnol.* **2019**, *14*, 12.

[3] P. Albert, K. Mark, G. E. C., E. Bruno, S. W. C., *Science (80-.).* **2016**, *352*, aad4424.

[4] D. C. Marinica, A. G. Borisov, S. V. Shabanov, *Phys. Rev. Lett.* **2008**, *100*, 1.

[5] C. W. Hsu, B. Zhen, J. Lee, S. L. Chua, S. G. Johnson, J. D. Joannopoulos, M. Soljačić, *Nature* **2013**, *499*, 188.

[6] E. N. Bulgakov, A. F. Sadreev, *Phys. Rev. A* **2014**, *90*, 53801.

[7] E. N. Bulgakov, A. F. Sadreev, *Phys. Rev. A* **2015**, *92*, 23816.

[8] C. W. Hsu, B. Zhen, A. D. Stone, J. D. Joannopoulos, M. Soljačić, *Nat. Rev. Mater.* **2016**, *1*, 16048.

[9] A. F. Sadreev, *Reports Prog. Phys.* **2021**, *84*, 55901.

[10] A. Kodigala, T. Lepetit, Q. Gu, B. Bahari, Y. Fainman, B. Kanté, *Nature* **2017**, *541*, 196.

[11] C. Huang, C. Zhang, S. Xiao, Y. Wang, Y. Fan, Y. Liu, N. Zhang, G. Qu, H. Ji, J. Han, L. Ge, Y. Kivshar, Q. Song, *Science (80-.).* **2020**, *367*, 1018 LP.

[12] S. T. Ha, Y. H. Fu, N. K. Emani, Z. Pan, R. M. Bakker, R. Paniagua-Domínguez, A. I. Kuznetsov, *Nat. Nanotechnol.* **2018**, *13*, 1042.

[13] S. I. Azzam, K. Chaudhuri, A. Lagutchev, Z. Jacob, Y. L. Kim, V. M. Shalaev, A. Boltasseva, A. V Kildishev, *Laser Photon. Rev.* **2021**, *15*, 2000411.

[14] M.-S. Hwang, H.-C. Lee, K.-H. Kim, K.-Y. Jeong, S.-H. Kwon, K. Koshelev, Y. Kivshar, H.-G. Park, *Nat. Commun.* **2021**, *12*, 4135.

[15] S. Romano, M. Mangini, E. Penzo, S. Cabrini, A. C. De Luca, I. Rendina, V. Mocella, G. Zito, *ACS Nano* **2020**, *14*, 15417.

[16] A. Tittl, A. Leitis, M. Liu, F. Yesilkoy, D.-Y. Choi, D. N. Neshev, Y. S. Kivshar, H. Altug, *Science (80-.).* **2018**, *360*, 1105.

[17] A. Leitis, A. Tittl, M. Liu, B. H. Lee, M. B. Gu, Y. S. Kivshar, H. Altug, *Sci. Adv.* **2019**, *5*, eaaw2871.

[18] I.-C. Benea-Chelmus, S. Mason, M. L. Meretska, D. L. Elder, D. Kazakov, A. Shams-Ansari, L. R. Dalton, F. Capasso, *Nat. Commun.* **2022**, *13*, 3170.

[19] L. Xu, K. Zangeneh Kamali, L. Huang, M. Rahmani, A. Smirnov, R. Camacho-Morales, Y. Ma, G. Zhang, M. Woolley, D. Neshev, A. E. Miroshnichenko, *Adv. Sci.* **2019**, *6*, 1802119.

[20] Z. Liu, Y. Xu, Y. Lin, J. Xiang, T. Feng, Q. Cao, J. Li, S. Lan, J. Liu, *Phys. Rev. Lett.* **2019**, *123*, 253901.

[21] K. Koshelev, Y. Tang, K. Li, D.-Y. Choi, G. Li, Y. Kivshar, *ACS Photonics* **2019**, *6*, 1639.

[22] K. Koshelev, S. Kruk, E. Melik-Gaykazyan, J.-H. Choi, A. Bogdanov, H.-G. Park, Y. Kivshar, *Science (80-.).* **2020**, *367*, 288 LP.

[23] I. A. M. Al-Ani, K. As'Ham, L. Huang, A. E. Miroshnichenko, H. T. Hattori, *Laser Photon. Rev.* **2021**, *15*, 2100240.

[24] I. A. M. Al-Ani, K. As'Ham, L. Huang, A. E. Miroshnichenko, W. Lei, H. T. Hattori, *Adv. Opt. Mater.* **2022**, *10*, 2101120.

[25] K. L. Koshelev, S. K. Sychev, Z. F. Sadrieva, A. A. Bogdanov, I. V Iorsh, *Phys. Rev. B* **2018**, *98*, 161113.

[26] V. Kravtsov, E. Khestanova, F. A. Benimetskiy, T. Ivanova, A. K. Samusev, I. S. Sinev, D. Pidgayko, A. M. Mozharov, I. S. Mukhin, M. S. Lozhkin, Y. V Kapitonov, A. S. Brichkin, V. D. Kulakovskii, I. A. Shelykh, A. I. Tartakovskii, P. M. Walker, M. S. Skolnick, D. N. Krizhanovskii, I. V Iorsh, *Light Sci. Appl.* **2020**, *9*, 56.

[27] M. Qin, S. Xiao, W. Liu, M. Ouyang, T. Yu, T. Wang, Q. Liao, *Opt. Express* **2021**, *29*, 18026.

[28] B. Zhen, C. W. Hsu, L. Lu, A. D. Stone, M. Soljačić, *Phys. Rev. Lett.* **2014**, *113*, 257401.

[29] A. C. Overvig, S. C. Malek, N. Yu, *Phys. Rev. Lett.* **2020**, *125*, 17402.

[30] A. Overvig, A. Alù, *Adv. Photonics* **2021**, *3*, 1.

[31] A. Overvig, N. Yu, A. Alù, *Phys. Rev. Lett.* **2021**, *126*, 73001.

[32] W. Liu, B. Wang, Y. Zhang, J. Wang, M. Zhao, F. Guan, X. Liu, L. Shi, J. Zi, *Phys. Rev. Lett.* **2019**, *123*, 116104.

[33] M. V Gorkunov, A. A. Antonov, Y. S. Kivshar, *Phys. Rev. Lett.* **2020**, *125*, 93903.

[34] B. Wang, W. Liu, M. Zhao, J. Wang, Y. Zhang, A. Chen, F. Guan, X. Liu, L. Shi, J. Zi, *Nat. Photonics* **2020**, *14*, 623.

[35] K. Koshelev, S. Lepeshov, M. Liu, A. Bogdanov, Y. Kivshar, *Phys. Rev. Lett.* **2018**, *121*, 193903.

[36] V. A. Fedotov, M. Rose, S. L. Prosvirnin, N. Papasimakis, N. I. Zheludev, *Phys. Rev. Lett.* **2007**, *99*, 147401.

[37] L. Cong, R. Singh, *Adv. Opt. Mater.* **2019**, *7*, 1900383.

[38] L. Xu, M. Rahmani, Y. Ma, D. A. Smirnova, K. Z. Kamali, F. Deng, Y. K. Chiang, L. Huang, H. Zhang, S. Gould, D. N. Neshev, A. E. Miroshnichenko, *Adv. Photonics* **2020**, *2*, 1.

[39] D. R. Abujetas, N. van Hoof, S. ter Huurne, J. Gómez Rivas, J. A. Sánchez-Gil, *Optica* **2019**, *6*, 996.

[40] J.-H. Yang, Z.-T. Huang, D. N. Maksimov, P. S. Pankin, I. V Timofeev, K.-B. Hong, H. Li, J.-W. Chen, C.-Y. Hsu, Y.-Y. Liu, T.-C. Lu, T.-R. Lin, C.-S. Yang, K.-P. Chen, *Laser Photon. Rev.* **2021**, *15*, 2100118.

[41] S. Campione, S. Liu, L. I. Basilio, L. K. Warne, W. L. Langston, T. S. Luk, J. R. Wendt, J. L. Reno, G. A. Keeler, I. Brener, M. B. Sinclair, *ACS Photonics* **2016**, *3*, 2362.

[42] S. Liu, A. Vaskin, S. Addamane, B. Leung, M.-C. Tsai, Y. Yang, P. P. Vabishchevich, G. A. Keeler, G. Wang, X. He, Y. Kim, N. F. Hartmann, H. Htoon, S. K. Doorn, M. Zilk, T. Pertsch, G. Balakrishnan, M. B. Sinclair, I. Staude, I. Brener, *Nano Lett.* **2018**, *18*, 6906.

[43] S. Li, C. Zhou, T. Liu, S. Xiao, *Phys. Rev. A* **2019**, *100*, 63803.

[44] C. Cui, C. Zhou, S. Yuan, X. Qiu, L. Zhu, Y. Wang, Y. Li, J. Song, Q. Huang, Y. Wang, C. Zeng, J. Xia, *ACS Photonics* **2018**, *5*, 4074.

[45] C. Zhou, X. Qu, S. Xiao, M. Fan, *Phys. Rev. Appl.* **2020**, *14*, 44009.

[46] L. Huang, Y. Yu, L. Cao, *Nano Lett.* **2013**, *13*, 3559.

[47] L. Huang, L. Xu, M. Rahmani, D. Neshev, A. E. Miroshnichenko, *Adv. Photonics* **2021**, *3*, DOI 10.1117/1.AP.3.1.016004.

[48] L. Huang, G. Li, A. Gurarslan, Y. Yu, R. Kirste, W. Guo, J. Zhao, R. Collazo, Z. Sitar, G. N. Parsons, M. Kudenov, L. Cao, *ACS Nano* **2016**, *10*, 7493.

[49] V. R. Tuz, V. V Khardikov, A. S. Kupriianov, K. L. Domina, S. Xu, H. Wang, H.-B. Sun, *Opt. Express* **2018**, *26*, 2905.

[50] P. C. Wu, C. Y. Liao, V. Savinov, T. L. Chung, W. T. Chen, Y.-W. Huang, P. R. Wu, Y.-H. Chen, A.-Q. Liu, N. I. Zheludev, D. P. Tsai, *ACS Nano* **2018**, *12*, 1920.

[51] V. Savinov, V. A. Fedotov, N. I. Zheludev, *Phys. Rev. B* **2014**, *89*, 205112.

[52] P. Grahn, A. Shevchenko, M. Kaivola, *New J. Phys.* **2012**, *14*, 93033.

[53] J. Jin, X. Yin, L. Ni, M. Soljačić, B. Zhen, C. Peng, *Nature* **2019**, *574*, 501.

[54] M. Galli, S. L. Portalupi, M. Belotti, L. C. Andreani, L. O'Faolain, T. F. Krauss, *Appl. Phys. Lett.* **2009**, *94*, 71101.

[55] A. E. Miroshnichenko, S. Flach, Y. S. Kivshar, *Rev. Mod. Phys.* **2010**, *82*, 2257.